Electronic structures and spectroscopic signatures of silicon-vacancy containing nanodiamonds

Alessio Petrone, Ryan A. Beck, Joseph M. Kasper, Xiaosong Li, Yue Huang, Matthew Crane, and Peter Pauzauskie

Phys. Rev. B **98**, 205405 — Published 8 November 2018

DOI: 10.1103/PhysRevB.98.205405

Electronic Structures and Spectroscopic Signatures of Silicon-Vacancy Containing Nanodiamonds

Alessio Petrone,* Ryan A. Beck,* Joseph M. Kasper, and Xiaosong Li†
Department of Chemistry, University of Washington, Seattle, WA, 98195

Yue Huang, Matthew Crane, and Peter Pauzauskie
Department of Materials Science and Engineering, University of Washington, Seattle, WA, 98195
(Dated: October 16, 2018)

The presence of mid-gap states introduced by localized defects in wide-band-gap doped semiconductors can strongly affect the electronic structure and optical properties of materials, generating a wide range of applications. Silicon-divacancy defects in diamond have been recently proposed for probing high-resolution pressure changes and performing quantum cryptography, making them good candidates to substitute the more common nitrogen-vacancy centers. Using group theory and *ab initio* electronic structure methods, the molecular origin of mid-gap states, zero phonon line splitting and size dependence of the electronic transitions involving the SiV center is investigated in this work. The effects of localized defects on the Raman vibrational and carbon K-edge X-ray absorption spectra are also explored for nanodiamonds. This paper presents an important analysis of the electronic and vibrational structure of nanosized semi-conductors in the presence of mid-gap states due to localized defects, providing new insights into possible mechanisms for modulating their optical properties.

I. INTRODUCTION

Wide-band-gap doped semiconductors are promising candidates for use in many technological applications since the controlled implantation of localized defects can introduce new electronic levels within the band gap, strongly modifying the material interactions with electromagnetic radiation.[1–6] Diamond presents a large optical band gap for bulk (∼5.5 eV)[7] and has a very dense lattice that both restricts defect diffusion and phase transitions at high temperatures. Thus, the manipulation and the characterization of isolated defects in diamonds have generated a wide range of applications such as quantum computing, sensing, and cryptography.[8–14]

When the crystal size approaches the nano-dimension (∼5 nm), diamonds no longer express bulk properties. A band gap opening is observed and discrete electronic levels (typical of molecules) emerge at band edges. These are all consequences of the quantum confinement effect.[15–18] Therefore, the interaction between doped diamonds and light may be further modulated by adjusting the host nanocrystal size. Substitutional nitrogen and nitrogen-vacancy centers are common defects in diamond and have received attention for their sensitive optical and spin properties.[8–11,19–21] The peculiar low diffusion rate of NV centers enables the optical probing of local variations in time, which can affect the spin precession rate of the defects, making them suitable for quantum sensing applications.[14] Doping introduces new sub-band-gap levels, and it has been shown that NV centers in diamond give rise to new dopant-centered $sp^3 - sp^3$ mid-gap electronic transitions and charge-transfer (CT or "photoionization") excited states.[22] Similar applications in quantum information processing[23] have been shown for the negatively-charged silicon-vacancy (SiV^-) center due to its short fluorescent lifetime, narrow emission linewidth, and high percentage of photons (∼70-80%) emitted through its zero-phonon line (ZPL).[24,25] This defect has also been shown to be useful as a high-resolution high-pressure sensor.[26] Doped diamond based pressure probes can function at higher pressures than the currently used ruby sensors, as the rigid diamond lattice is still present above 100 GPa, while ruby undergoes a phase transition.

The SiV center can exist as either a neutral triplet in its ground state, neutral SiV , or as an anionic doublet state, anionic SiV^-.[27–31] The latter is the most common stable ground state electronic configuration[32]. Experimentally, the ZPL measured in doped diamonds in the bulk limit is 1.31 eV and 1.68 eV for the neutral SiV and anionic SiV^-, respectively. Additionally, in SiV^- a blue-shift in the zero phonon line as a function of the decreasing crystal size has been observed for nanodiamonds.[33] For the reduced systems the ZPL splits into a four-line fine-structure at helium temperature[34,35]. The origin of this fine structure splitting in the ground and excited states has been explained by dynamic Jahn-Teller and/or by spin-orbit effects.[27,34,36,37]

Vibrational spectroscopy can also be used to probe the presence of these defects, since the changes in the dipole and the polarizability induced by the dopant can strongly modify the selection rules for the infrared and Raman active modes, respectively. In addition to UV-Vis, the K-edge X-ray absorption spectrum in diamonds has been proposed to be sensitive to the introduction of dopants.[38] Moreover, carbon K-edge spectra in nanodiamonds exhibit unidentified pre-edge features that have been either attributed to the presence of sp^2 carbon atoms lying on the surface, as a consequence of the surface reconstruction, or to the introduction of new empty levels within the band gap resulting from impurities.[38] Despite their importance, carbon K-edge X-ray and vi-

brational transitions for the characterization of SiV centers in nanodiamond, along with the effects of the SiV center location in the crystal lattice (i.e. surface effects, symmetry breaking) and system size (i.e. quantum confinement) on the electronic and vibrational excitations, have not been well studied. In this paper, theoretical investigations with a finite cluster approach of both the electronic and vibrational properties are carried out using hybrid density functional theory (DFT) and linear-response time-dependent density functional theory (LR-TDDFT) for a reduced SiV^- color center in nanodiamond systems of different sizes. TDDFT, combined with a cluster approach, has shown very promising results for the theoretical characterization of excited states in doped semi-conductor quantum dots (in particular, NV doped nanodiamonds)[22,39–48] and the vibrational/dynamical properties of molecules.[49–53] The work presented herein focuses on the quantum confinement effects on the electronic (UV-Vis and X-ray) and vibrational (Raman) spectroscopies on several SiV-doped diamond nanoclusters. The effect of the defect symmetry (or the lack of) as a function of the size is also analyzed.

II. METHODOLOGY

Nearly spherical diamond quantum dots, $C_{44}H_{42}$ (diameter ∼0.8 nm), $C_{121}H_{104}$ (diameter ∼1.2 nm), $C_{182}H_{142}$ (diameter ∼1.4 nm), and $C_{487}H_{310}$ (diameter ∼2.1 nm) were used as starting models for the SiV doped systems. They were constructed using the bulk face-centered cubic lattice parameter[7] $a_0 = 0.357$ nm and hydrogen atoms were used to passivate the surface dangling bonds, according to the procedure presented in Ref. 22. The sizes of these quantum dots are similar to the smallest nano-diamonds obtainable by detonation or laser-heated diamond anvil cell synthesis.[12,54–56] As the diamond excitonic Bohr radius is estimated to be ∼1.6 nm,[57] electronic properties of these small diamond quantum dots will exhibit quantum confinement effects.

The SiV center in diamond consists of a silicon atom and a vacancy in a split-vacancy configuration.[28,30,58] The SiV center was created by removing two carbon atoms near the center of the nanodiamonds along the $< 1, 1, 1 >$ axis of the models, and positioning the silicon at the center of the resulting divacancy in a local D_{3d} environment (namely SiV *frozen*), as observed in previous computational studies.[27,31,59,60] To evaluate the lattice distortion due to the presence of the SiV center itself, the SiV center and the nearest neighboring six carbon atoms were fully optimized while maintaining the rest of the diamond structure at the crystal lattice (namely SiV *relaxed*). These optimization schemes have shown accurate results for describing the lattice distortion of nitrogen-vacancy doped diamonds of similar sizes.[22] In this work, we focus on the reduced SiV^- center, whose ground state has been shown to be a doublet.[32] The ∼1.2 nm reduced SiV^- $C_{119}SiH^-_{104}$ was used to estimate the excited state structural reorganization and relaxation energy. This system was further optimized according the first bright excited state energy gradient provided by TDDFT and using the SiV^- *relaxed* optimization scheme, described above. The relaxation energy in the excited state was computed as the energy difference between the vertical excitation energy using the ground state and the excited state optimized geometries. The ∼1.2 nm diameter pure $C_{121}H_{104}$, and the reduced SiV^- $C_{119}SiH^-_{104}$, were also further fully optimized in the ground state by relaxing all atoms to perform the vibrational analysis. Geometries were considered fully optimized when both the forces (maximum and RMS force, 0.000450 and 0.000300 Hartree/bohr, respectively) and displacement (maximum and RMS displacement, 0.0018 and 0.0012 bohr, respectively) values for all free atoms were below the threshold criteria.

All calculations were performed using the development version of the Gaussian software package.[61] The ground state electronic structures were obtained by solving the Kohn-Sham equation using the range-separated version of hybrid Becke, 3-parameter, Lee-Yang-Parr (B3LYP) density functional[62–64] with the Coulomb-attenuating approach (CAM-B3LYP).[65] The necessity of using basis sets with large spatial extent (i.e. diffuse functions) has been demonstrated to be important in nanodiamonds, since C-H bonds create low-energy empty states that are Rydberg-like, that may reduce the band gap.[66,67] These states can play an important role for shallow implanted NV centers in diamond.[68] On the other hand, diffuse functions have been previously shown to be less important for localized defects located far from the surface.[33,69,70] CAM-B3LYP is known to outperform canonical hybrid (i.e. B3LYP, PBE0, etc.) for the description of Rydberg-like and charge-transfer states due to their high sensitivity to the treatment of exact exchange.[71–73] Since the presence of these Rydberg-like states can influence the predicted quantum confinement effects, CAM-B3LYP/6-31++G(d,p) was used for this study. The electronic structures of excited states were calculated using TDDFT within the linear response framework[74–76] and its energy specific implementation for the high-energy states.[77,78]

III. RESULTS AND DISCUSSION

A. Structural Reorganization and Electronic Configurations

The models used in this work support local symmetry, but they do not preserve a global inversion symmetry operation, therefore the SiV *frozen* conformation has an overall C_{3v} symmetry, given the asymmetry on the nanodiamond surface. Effects of the SiV location in nanodiamonds (i.e. the position of the defect with respect to the surface) can also influence the electronic and optical properties of the systems and they are separately

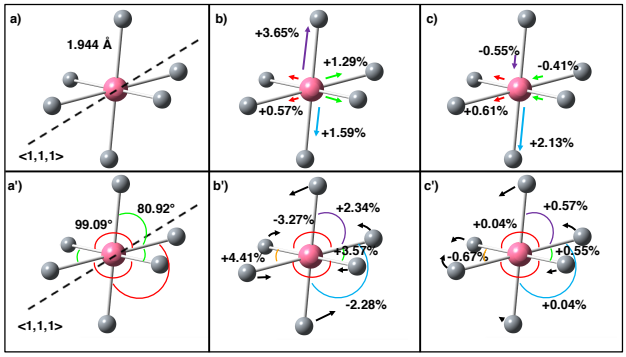

FIG. 1. Geometry relaxation near the SiV center for the ∼1.2 nm diameter reduced SiV^- $C_{119}SiH^-_{104}$ systems: carbon in grey, silicon in pink (only the active atoms during the optimization are reported, see methods for details). The SiV *frozen* structure with the silicon located in a pseudo-local D_{3d} symmetry (panels a and a′) is represented, along with the ground (panels b and b′) and first bright excited state (panels c and c′) relaxed structures. Both the bond (top panels) and the angle (bottom panels) change in value, upon relaxation (according to the procedure detailed in the methods) with respect to the SiV^- *frozen* configuration for the ground state and with respect to the ground state configuration for the excited state, are reported in percentages in panels b and c, respectively. The same color is used to highlight symmetric changes. The ground state *relaxed* geometry was also compared with the fully relaxed geometry showing a similar symmetry in the distortion (**??**).[79]

investigated in detail in the next sections for one of the larger models. Despite this, the models can retain, in the SiV *frozen* conformation, a local symmetric arrangement, where all Si-C distances are 1.944 Å and the C-Si-C angles are either 80.9° or 99.1°. The local symmetry of the defect may still be described as C_{3v} plus inversion, retaining a local D_{3d} symmetry (see Fig. 1, panels a and a′).

The lattice structural reorganization in the electronic ground state in d∼1.2 nm SiV doped nanodiamond is summarized in Fig. 1 (panels b and b′). A uniform expansion of the Si pocket can be clearly seen from the elongation of all Si-C distances. Upon relaxation on the ground electronic state, the local D_{3d} symmetry is broken, although a pseudo C_s symmetry can be still observed by inspecting the Si-C distances. When the system is further allowed to relax on the first bright excited state, a non-uniform bond change is observed. Half of the Si-C distances undergo an expansion of the bond length and the other half undergo a compression (see panel c in Fig. 1) compared to the previously examined ground state relaxed geometry. The calculated relaxation/reorganization energy due to the optical excitation for this size is about 0.01 eV, which is much smaller than the one observed for the NV center (about 0.21 eV). This value agrees with previous calculation on Si doped diamonds[30] and explains the small contribution of the vibration sideband in the emission spectrum for these systems.[32]

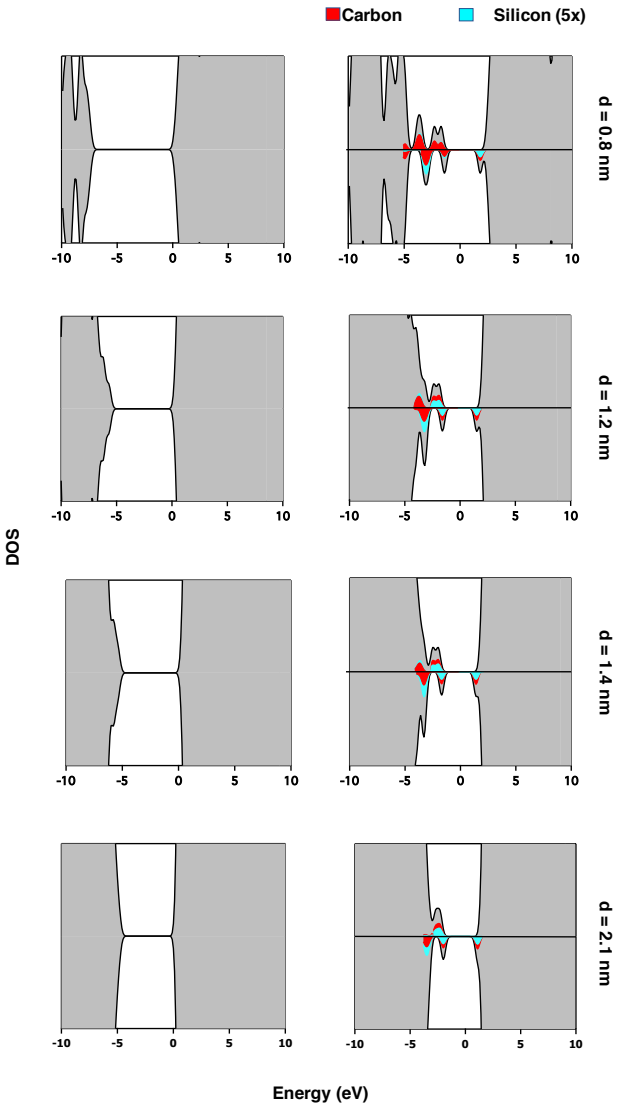

FIG. 2. CAM-B3LYP/6-31++G(d,p) DOS and PDOS (this last visualized only for Si and its first neighboring C atoms levels within the band gap and the CB). The red and light blue colored regions show the C $2p$ and Si (magnified by 5x) $3s$ and $3p$ contributions to the PDOS diagrams, respectively. Spin-up, positive density values; spin down, negative density values. The DOS diagrams are calculated for the pure C_XH_Y, and the reduced *frozen* $C_{X-2}SiH^-_Y$ (left and right, respectively) nanodiamonds of increasing sizes (d∼ 0.8, 1.2, 1.4, and 2.1 nm, from top to bottom).

Figure 2 shows the total and partial densities of states (PDOS) using the calculated molecular orbitals (MOs), with the spin-up and spin-down densities plotted as positive and negative values, respectively. Both the valence band (VB) and conduction band (CB) consist of carbon p and s characters, while multiple levels at the SiV center appear inside the band gap and near the band edges. The

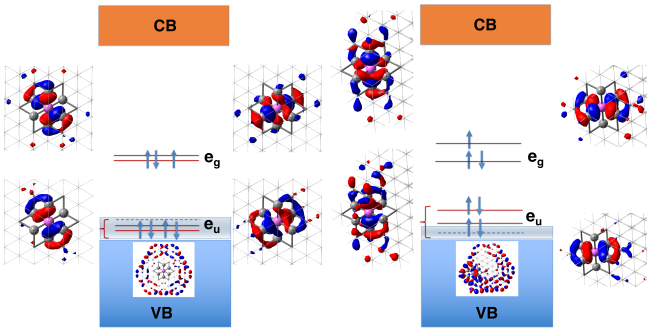

FIG. 3. Schematic illustration of the SiV center electronic layout, according to the D_{3d} point group symmetry. Panel a, SiV in the center of the nanodiamond, and panel b, where the SiV defect is close to the surface and partially breaks the group symmetry (position 1 and 4 in Fig. 6, respectively). The zoomed in $C_{180}SiH^{-}_{142}$ CAM-B3LYP/6-31++G(d,p) beta MOs contour plots with the pseudo C_{3v} axis parallel to the z-axis (entering the figure) are represented. The isodensity values of 0.05, 0.05 and 0.03 are used for the e_g, e_u and VB MOs contour plots, respectively. The energetic layout presents an uneven alignment between the alpha/beta filled e_g w.r.t. the beta e_g LUMO, please see Fig. 2 for a more detailed analysis.

VB and CB of the ∼2.1-nm-diameter nanodiamond are separated by an energy gap of 5.21 eV. As the system sizes decrease, the band gap increases due to stronger quantum confinement effects.

In the systems containing a SiV center, the silicon atom contributes its four valence electrons to the SiV center. There are also six dangling electrons from the six nearest-neighbor C atoms to the vacancies, giving rise to a total of ten electrons at the SiV center (eleven for the reduced system). The local D_{3d} symmetry splits the four sp^3 atomic orbitals of Si to a_{2u}, e_u, a_{1g}, and the six p atomic orbitals of nearby C atoms to e_g, e_u, a_{2u}, a_{1g} symmetry groups. The symmetry rules dictate that the set of orbitals of e_g symmetry has almost zero overlap with the Si atomic orbitals, resulting in a set of high energy (and mostly energetically "pinned" in the band gap) MOs with significant contributions from the carbon p orbitals surrounding the silicon (see colored PDOS in Fig. 2); all other atomic orbitals previously listed (e_g, e_u, a_{2u}, a_{1g}) can hybridize and form MOs surrounding the defect (depicted in Fig. 3(a)). The resulting σ bonding and antibonding MOs of a_{2u} and a_{1g} symmetry are energetically buried in the VB and CB, respectively (not shown).

On the other hand, the hybridized bonding MOs of e_u symmetry are the most interesting ones because they are likely responsible for the peculiar optical properties of SiV centers. These molecular orbitals lie at the VB edge (the antibonding ones are energetically located at the CB edge, not represented), and show a reasonable contribution from both the carbon p and silicon sp^3 orbitals. The resulting MOs show a non-zero overlap with the VB edge of the nanodiamonds, forming a set of three molecular orbitals at the VB edge. Only in the 0.8 nm nanodiamond the MOs of e_u symmetry are energetically well separated from the VB. In this work, the negatively charged SiV defect ground-state electronic state is ^2E_g (in a D_{3d} perfect symmetry) and its electronic configuration can be described as $e_u^4 e_g^3$, where the e_g level is partially filled, in agreement with previous DFT calculations.[27,30,80]

B. Midgap Optical Transitions

As the size of nanodiamond decreases, the quantum confinement effect[18,81] leads to an increase in the band-gap (5.21 eV for C_{487}, 5.78 eV for C_{182}, 6.07 eV for C_{121} and 7.77 eV for the C_{44}; reported as the HOMO/LUMO differences), as observed in other semiconducting nanocrystals.[39,82] The previously presented electronic structures for anionic SiV^- defects in nanodiamond give rise to several characteristic sets of optical transitions exhibited in spectroscopic measurement of SiV-containing nanodiamonds. Optical spectra for different sized SiV^- containing nanodiamonds using linear response TDDFT are reported in Fig. 4. The energy levels of these SiV centers in the diamond lattice are illustrated in Fig. 3(a). This energetic layout leads to unique midgap optical transitions in SiV-containing nanodiamonds.

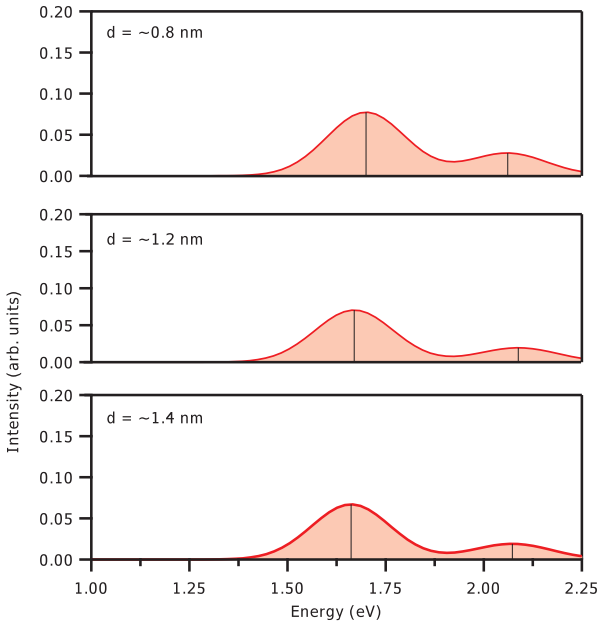

FIG. 4. TD-CAM-B3LYP/6-31++G(d,p) UV-Vis spectra (only the two first mid-gap transitions involving the $e_u \rightarrow e_g$ beta manifold, are reported) for the relaxed anionic SiV^- $C_{X-2}SiH^-_Y$ nanodiamonds as a function of the increasing quantum dot diameter (d∼ 0.8, 1.2, and 1.4 nm from top to bottom). A Gaussian broadening has been applied to the individual transitions labeled with black lines to form the spectrum with a full width half maximum value of 0.10 eV.

The optical spectra in Fig. 4 shows an spectroscopic

feature between 1.70 and 2.10 eV consisting of two transitions, from the two filled MOs of e_u (β) symmetry to the empty e_g (β). Table I lists their vertical excitation energies in various SiV-containing nanodiamonds. These transitions give rise to the experimental zero-phonon line (ZPL) for the $^2E_g(e_u^4e_g^3) \rightarrow {}^2E_u(e_u^3e_g^4)$ excitation at 1.686 eV[32] and the main transition contributing to this feature undergoes a small blue shift with diminishing system size (from bottom to top in Fig. 4 and in Table I). The partial charge-transfer characters of the ZPL in SiV doped systems are due to the fact that MOs of e_u symmetry show a non-negligible delocalization along with a reasonable energy overlap with the VB edge (these last levels have a higher contribution arising from surface carbons, see Fig. 3(a)), as can be inspected from the computed DOS in Fig. 2.

TABLE I. TD-CAM-B3LYP/6-31++G(d,p) mid-gap vertical excitation energies (e_u to e_g, beta manifold) for the anionic SiV^- systems (in eV) and the corresponding oscillator strengths (reported in parenthesis). All systems present a dark excited excited state <100 meV apart from the ground state, due to the swap between the occupied and empty e_g orbitals (transitions not shown). We compare results between the SiV *relaxed* (SiV center position is optimized, see text) with the ones obtained from just inserting the SiV center by replacing the corresponding atoms (SiV *frozen*) in the center of the pure nanodiamond.

	SiV *relaxed*	SiV *frozen*
SiV^- $C_{42}SiH_{42}^-$	1.70(0.077)	1.63(0.068)
	2.06(0.028)	1.81(0.014)
SiV^- $C_{119}SiH_{104}^-$	1.67(0.070)	1.59(0.061)
	2.09(0.019)	1.82(0.014)
SiV^- $C_{180}SiH_{142}^-$	1.59(0.064)	1.51(0.056)
	1.99(0.021)	1.90(0.015)

The quantum confinement effect on the spectral shift of the ZPL (ΔE_{ZPL}) as a function of the band-to-band-excitonic transition (ΔE_{EXC}) has the approximate relationship, according to the effective mass approximation for a spherical nanocrystal:[17,39,42]

$$\Delta E_{\mathrm{ZPL}} \approx \frac{m_e^{*-1}}{m_e^{*-1} + m_h^{*-1}} \Delta E_{\mathrm{EXC}} \qquad (1)$$

where m_e^* and m_h^* are the effective masses (in units of electron mass) of the electron and hole in the SiV-containing nanodiamond. The ^2E_g $(e_u^4e_g^3) \rightarrow {}^2E_u$ $(e_u^3e_g^4)$ excitations (as a weighted average of the first two excitations in Table I) as a function of the band-to-band-excitonic transition for the different dot sizes is plotted in Fig. 5. The $\Delta E_{\mathrm{ZPL}}/\Delta E_{\mathrm{EXC}}$ value is 0.04, less than that in NV doped nanodiamonds,[22] and is significantly smaller than those for the free CB electron in diamond quantum dots. The observed size dependence of the ZPL is comparable with the one predicted using similar dimensions and level of theory.[33] Moreover, the quantitative analysis presented here, suggests that the photoexcited electrons in the SiV ZPL excited states of diamonds are "heavier" than those in the pure diamond excitonic states.

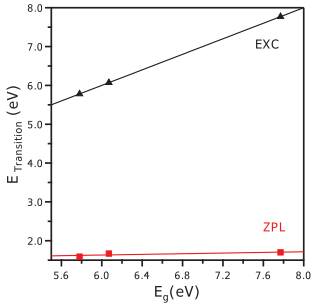

FIG. 5. TD-CAM-B3LYP/6-31++G(d,p) SiV ^2E_g $(e_u^4e_g^3) \rightarrow {}^2E_u$ $(e_u^3e_g^4)$ ZPL excitations, as a function of the band-to-band-excitonic transition, for the anionic SiV^- systems. Extrapolation of the ZPL energies gives a value of 1.38 eV for the bulk and the ratio between ΔE_{ZPL} and ΔE_{EXC} as the slope of the linear fit is 0.04 (The reported EXC energy (band gap) is reported as a HOMO/LUMO difference, which can underestimate the experimentally observed optical band gap as it has not been computed at the TD-DFT level of theory, and also can be affected by the presence of surface defects in the experiment).

C. Symmetry (or the lack of)

The two MOs of e_u symmetry have different spatial extent (i.e. different symmetry along the x and y directions, see Fig. 3(a)) and subsequently different overlaps with the empty MOs of e_g symmetry, showing different relative intensities in their transitions, as can be inferred by inspecting computed oscillator strength values reported for different sized SiV-doped nanodiamonds in Table I. By analyzing these values for the SiV *frozen* systems (right columns in Table I), an average splitting of ~0.27 eV is already noticed for the computed $^2E_g(e_u^4e_g^3) \rightarrow^2 E_u(e_u^3e_g^4)$ excitations. As mentioned before, although the SiV *frozen* conformation has an overall C_{3v} symmetry, both the asymmetry in the surface and the different spatial overlap of the filled MOs of e_u symmetry with the VB can be responsible for the energy splitting in the two $^2E_g(e_u^4e_g^3) \rightarrow^2 E_u(e_u^3e_g^4)$ transitions even in these *frozen* conformations (see the different overlap with the VB in Fig. 3(a)). The asymmetric overlap between e_u MOs with the VB is, therefore, the key reason for both the excitonic behavior (analyzed in the previous paragraph) and the asymmetry of the absorption peak in the visible range for the SiV doped systems. A similar interpretation has been previously provided for silicon

doped nanodiamonds of similar dimensions.[33]

The effect of lattice reorganization on the $^2E_g(e_u^4e_g^3) \rightarrow {}^2E_u(e_u^3e_g^4)$ excitations as a function of the system size can be also analyzed in Table I (from right to left). The geometry reorganization is responsible for an additional blue shift in vertical excitation energies, from ∼0.07 (first excitation) to ∼0.25 eV (second excitation), with respect to the unrelaxed conformations. The degree of splitting of the two $^2E_g(e_u^4e_g^3) \rightarrow {}^2E_u(e_u^3e_g^4)$ excitations for the SiV *relaxed* systems are comparable to the ones computed for the SiV *frozen*, suggesting that the interactions of these levels with the VB band and surface are already significant to induce asymmetry in these excitations even in the SiV *frozen* doped systems.

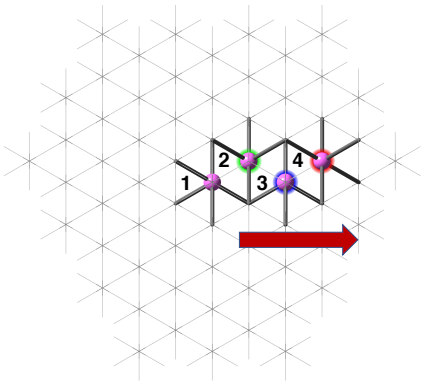

FIG. 6. Four different SiV positions the $C_{180}SiH_{142}^-$ system are investigated for anisotropic effects on SiV mid-gap optical transitions

TABLE II. TD-CAM-B3LYP/6-31++G(d,p) mid-gap vertical excitation energies (e_u to e_g, beta manifold) for the anionic SiV^- systems (in eV)as a function of the SiV center position moving from the center (position 1) towards the surface (position 4) for the $C_{180}SiH_{142}^-$ system. Results are compared between the SiV *relaxed* (SiV center position is optimized, see text) with the ones obtained by just inserting the SiV center by replacing the corresponding atoms (SiV *frozen*) in the center of the pure nanodiamond.

	SiV *relaxed*	SiV *frozen*
Position 1	1.59	1.51
	1.99	1.90
Position 2	1.66	1.67
	2.07	2.07
Position 3	1.69	1.67
	2.12	2.07
Position 4	1.67	1.60
	2.05	2.00

Since the relative position of the SiV defect with respect to the nanodiamond surface can further perturb the overall symmetry of the system, we inspected how the location of the SiV center within the nanodiamond can affect the SiV ZPL transitions. As the SiV center moves away from the C_{3v} (pseudo-local D_{3d} in SiV *frozen* systems) symmetry center, its global symmetry is no longer C_{3v}. As a result, the set of MOs of e_u and e_g symmetry, as shown in Fig. 3(b), are even more energetically different due to the different interactions of the x and y subset of the e_u and e_g MOs (see their asymmetric distributions in Fig. 3(b)) as the SiV moves closer to the surface (e.g., positions 2-4 in Fig. 6). The consequence of the symmetry breaking due to the defect position on ^2E_g $(e_u^4e_g^3) \rightarrow {}^2E_u$ $(e_u^3e_g^4)$ excitations is summarized in Table II. A splitting of ∼ 400 meV of SiV midgap transitions is observed when the SiV moves away from the C_{3v} center of the nanodiamond for the SiV *frozen*. The magnitude of the splitting is not very sensitive to the defect position with respect to the surface, although the overall values show an overall 0.1 eV blue shift for the SiV positions closest to the surface (larger if the systems are allowed to relax, as can be determined by looking at the values on the left in the table). This splitting of midgap transitions has been previously shown to be sensitive to the defect position relative to the surface, but its absolute value for SiV defects appears to be larger than for the NV center.[22] Both the SiV^- peak position and broadening of the emission line-width have experimentally been proved to be sensitive to either uniaxial stress or the position of the center within the matrix, in a similar way to the predicted values (∼200 meV in some observed broadenings).[83–85] As the ZPL is sensitive to the surface reorganization and the size of the system, SiV centers can be effective probes of the global and local distortions, i.e. mechanical stress or pressure.

D. Vibrational Analysis

Vibrational spectroscopy can be very sensitive to the presence of defects, since localized defects can strongly change the selection rules for infrared and Raman active modes. Presented in Fig. 7 is the Raman spectrum for the 1.2 nm pure (black) and reduced SiV^- (blue) nanodiamond. Given the system size and the high computational cost of Raman calculations, a less expensive 6-31G(d) basis set was utilized for frequency and Ramon intensity calculations. This choice is based on the observation that fully optimized geometries using 6-31++G(d,p) and 6-31G(d) bases show negligible differences, especially at the defect center. For the calculation of the vibrational response, it has been noted that, for large systems, this level of theory is sufficient,[86–89] although Raman intensity can be improved with additional diffuse function. The energy range discussed covers the region mostly affected by the presence of the SiV defects (the C-H stretching modes localized on the surface at $\sim> 3000$ cm^{-1} are not represented). Two distinctive

regions can be located by observing the Raman spectrum: the region between 1200 and 1650 cm^{-1}, involving surface H-C-H bending motions covering the typical diamond Raman band around 1300 cm^{-1} (due to the lattice C-C stretching), and the low frequency modes between ∼150 and ∼450 cm^{-1}, involving collective lattice breathing modes. The separation of these two regions has been showed to be sensitive to both the size and shape of nanodiamonds.[90]By introducing the SiV defect, an overall increase of the signal response in the region below 1100 cm^{-1} is observed. The main vibrational signatures of the presence of the SiV defect seem to be located around ∼910 and ∼156 cm^{-1}. These modes have a high contribution from the Si atom: the first are still collective stretching modes of the lattice in which C-Si are also strongly involved, while the lower energy ones are the vacancy stretching breathing modes (see Fig. 8 for their representations). This last spectral region seems to be the most sensitive to the isotopic substitution of the silicon atom as can be inferred by the examination of Fig. 9(a), where the isotopic pure Raman spectra for the most abundant isotopes of silicon is reported (^{28}Si, ^{29}Si, and ^{30}Si from top to bottom of the left panel). A progressive red shift of ∼1.5 cm^{-1} is observed for the peak around ∼156 cm^{-1} for each increase of the silicon atomic mass. In addition, the breathing mode at ∼442 cm^{-1} (marked in red in Fig. 9(a) and represented in Fig. 9(b)) strongly shows a decrease in intensity as an effect of the isotopic mass increment. Vibrational Raman responses associated with the anionic SiV^- and the Si substitutional defect were also compared. The substitutional defect was obtained by replacing a carbon atom close to the center of the ∼1.2 nm pure nanodiamond with a Si atom and optimizing the resulting structure. The SiV^- shows very distinct vibrational responses with respect to both the pure and the substitutional one (**??**).[79]

Unfortunately, the spectral region presenting the typical diamond Raman peak, involving the C-C lattice stretching motions reported at ∼1330 cm^{-1} for bulk diamonds[91–93], is completely washed out the by H-C-H bending motions, due to the hydrogen passivation of the surface. This problem is solved by setting the atomic mass of hydrogen to a large value (100 amu), which corresponds effectively to shift away the overlapping features from the studied spectral window.[48,90,94] The obtained Raman spectra using heavy hydrogen atoms (from 800 to 1600 cm^{-1}) are reported in insets of Fig. 7. The pure nanodiamond presents a sharp peak around ∼1310 cm^{-1}, due to the C-C lattice stretching motions (see Fig. 8). This is the typical diamond Raman fingerprint and it is 20 cm^{-1} red shifted with respect the experimental bulk phonon band.[90,94] The SiV doped spectrum shows a broadening of this peak, where several lattice stretching C-C motions involving carbon atoms around the SiV are now gaining intensity due to the presence of the Si, related to changes in the polarizability for these modes. These results are in agreement with the broadening observed for Raman spectra of Si doped diamonds.[95–97]

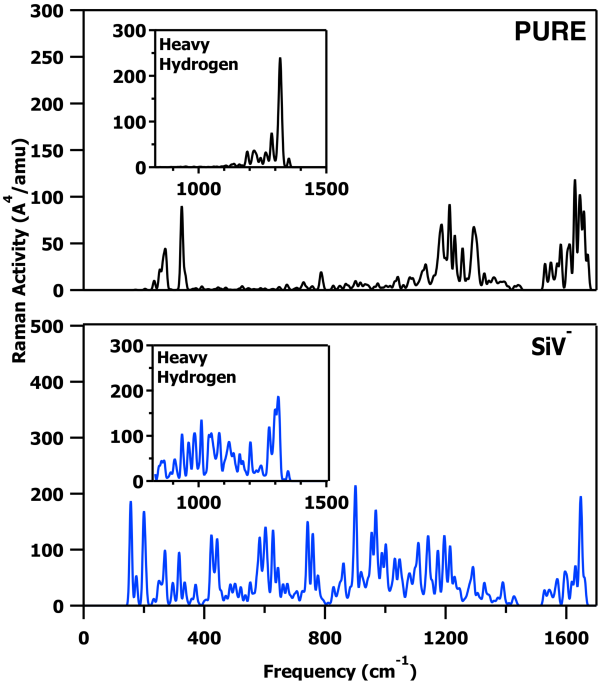

FIG. 7. CAM-B3LYP/6-31G(d) calculated Raman spectra for the ∼1.2 nm diameter pure $C_{121}H_{104}$ (black), and the reduced (isotopically averaged) SiV^- $C_{119}SiH^-_{104}$ fully optimized nanodiamonds (blue). A Gaussian broadening has been applied with a full width half maximum value of 4 cm^{-1}. Insets of the spectral window originally overlapping with the H-C-H modes (from 800 to 1600 cm^{-1}) obtained using artificially heavy hydrogen atoms (100 amu) are reported for both spectra. The Raman spectrum for Si substitutional defect can be found in the supplementary information (**??**).[79]

E. X-ray Absorption Spectroscopy

X-ray absorption spectroscopy (XAS) is extensively used for sample analysis, since it is a highly element specific spectroscopic technique. The K-edge feature in the XAS is due to the excitations involving $1s$ core electrons and the virtual valence molecular orbitals, for these reasons the structure of these peaks can provide useful information on the local order around the absorbing centers.[99–102] The resulting carbon K-edge X-ray absorption spectra for the ∼1.2 nm diameter pure $C_{121}H_{104}$ and the reduced SiV^- $C_{119}SiH^-_{104}$ nanodiamonds are reported in Fig. 10. The pure nanodiamond presents a clear absorption peak starting at 290 eV due to the well studied $1s \rightarrow \sigma^*$ transitions. As the SiV is introduced, several pre-edge transitions start to appear around 284 − 285 eV. The main peak at ∼290 eV for the Si doped systems is still due to several $1s \rightarrow \sigma^*$ electronic transitions, as can be inferred by inspecting the MOs responsible for them in both the pure and doped systems (see their representation in Fig. 10). The pre-edge peaks around 285 eV are due to the presence of the SiV defects, arising from several carbon $1s \rightarrow e_g$ transitions (see Fig. 10).

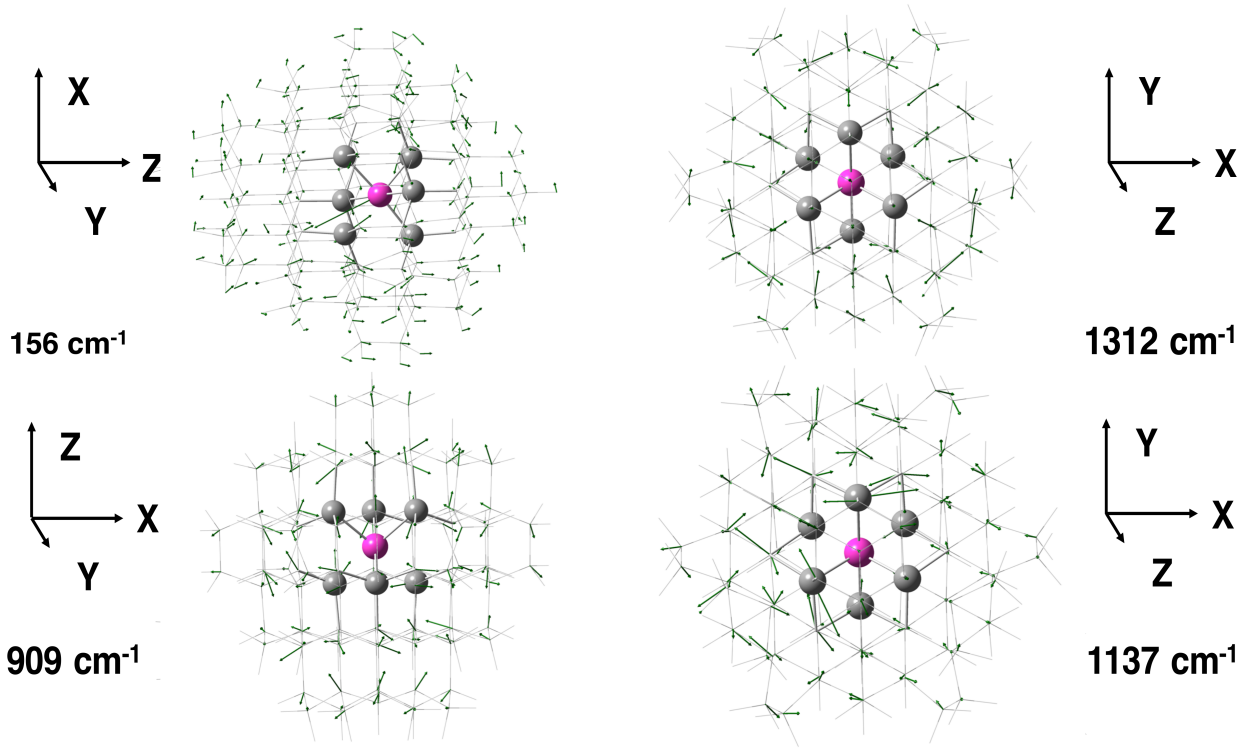

FIG. 8. Displacement vectors of the most representative normal modes for the ∼1.2 nm diameter SiV^- $C_{119}SiH^-_{104}$ doped fully optimized nanodiamond. The modes within the 909 to 1137 cm^{-1} energy range are represented using the 'heavy hydrogen' approximation for clarity, while the lowest pictured mode at 156 cm^{-1} is shown with the regularly massed system. Representations of the individual modes are also provided in ????????.[79]

These analyses suggest that the pre-edge feature experimentally observed at ∼ 285 eV can be a signature of the presence of defects (i.e. SiV centers). While these carbon transitions are typically ascribed to sp^2 carbon atoms lying on the surface,[48] it should be noted that these are also available to the dangling bonds surrounding carbon vacancies. However, in defects like NV and SiV, the presence of heteroatoms influences the $1s \rightarrow e_g$ carbon transition. Thus, the location of the carbon K-edge pre-edge features can be used to probe the presence of different dopants in diamonds.[38]

IV. CONCLUSION

In this work, the mid-gap states introduced by localized defects have been shown to affect UV-Vis, X-ray and vibrational transitions in diamonds approaching the nanoscale. Using group theory and DFT electronic structure, we showed how the mid-gap states introduced by the reduced SiV center have a non-negligible overlap with the diamond VB and CB. This explains the size dependent nature of the computed SiV ZPL and we predict an effective excitonic mass for these transitions comparable to charge transfer excitations in NV doped nanodiamonds. We also found the ZPL to be sensitive both to the lack of symmetry in all systems analyzed and to the defect position by measuring the band position, during the defect migration towards the surface. Two diamond Raman vibrational spectrum regions are predicted to be significantly modified by the SiV center: the large amplitude breathing (120-450 cm^{-1}) and the stretching (800-1400 cm^{-1}) motions of the lattice. Core $1s \rightarrow e_g$ (mid-gap states) transitions introduced by SiV centers are predicted to be responsible for the occurrence of pre-edge peaks in the computed carbon K edge X-Ray absorption spectrum for nanodiamonds, showing for the first time how this spectral region (∼285 eV) can be influenced by the presence of localized defects. This work provides an important *ab initio* analysis of the electronic and vibrational structure of semi-conductors in the presence of mid-gap states due to localized defects, providing a molecular description of the spectroscopic changes in doped systems.

ACKNOWLEDGMENTS

The development of the energy-specific TDDFT method for computing XAS spectra is supported by the NSF (CHE-1565520 to XL). Study of defects in nanodiamond is supported by the University of Washington Molecular Engineering Materials Center (DMR-1719797) and NSF (CHE-1464497 to XL and NSF-

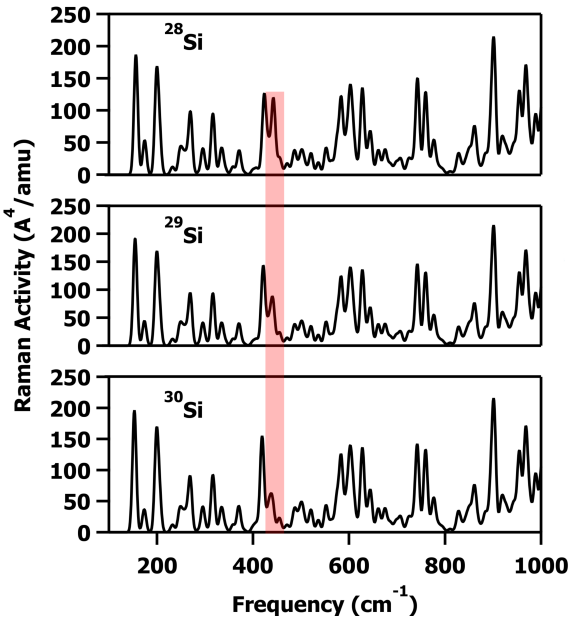

(a)

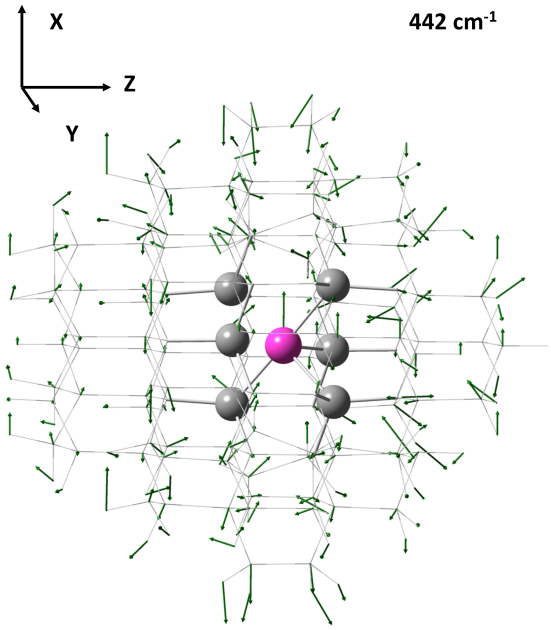

(b)

FIG. 9. (a) B3LYP/6-31G(d) isotopically pure calculated Raman spectra for the three most abundant[98] silicon isotopes ^{28}Si (92%), ^{29}Si (5%), and ^{30}Si (3%) from top to bottom of the left panel for the ∼1.2 nm diameter SiV^- $C_{119}SiH^-_{104}$ fully optimized nanodiamond. (b) displacement vectors of the most representative normal mode sensitive to the isotopic substitution.

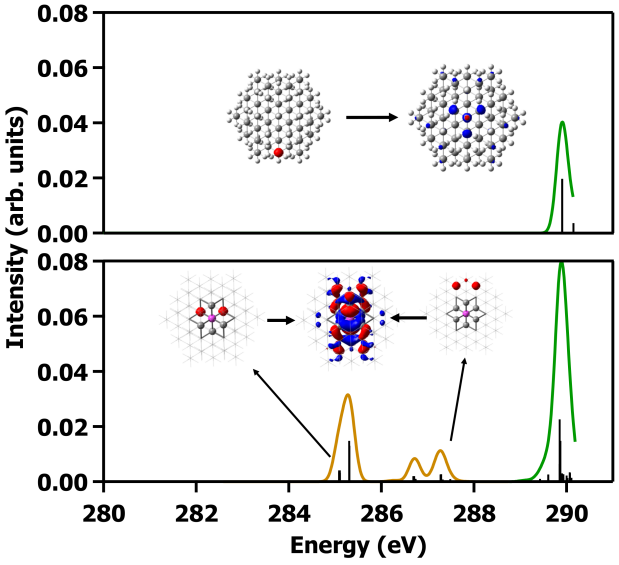

FIG. 10. TD-CAM-B3LYP/6-31++G(d,p) calculated XAS for the ∼1.2 nm diameter pure $C_{121}H_{104}$ (top, 10 states), and the reduced SiV^- $C_{119}SiH^-_{104}$ (bottom, 103 states) nanodiamonds. Carbon core $1s \rightarrow e_g$ and $1s \rightarrow \sigma^*$ transitions are grouped in orange and green, respectively. A Gaussian broadening has been applied to the individual transitions labeled with black lines to form the spectra with a full width half maximum value of 0.12 eV, and a uniform shift of 12 eV has been applied to the spectra to align theoretical results with experimental values. Contour plots of the molecular orbitals responsible for the carbon K-edge transitions, with the pseudo C_{3v} axis parallel to the z-axis (entering the figure) using an isodensity value of 0.025, are also represented.

CAREER 1555007 to PJP). This work was facilitated though the use of advanced computational, storage, and networking infrastructure provided by the Hyak supercomputer system and funded by the STF at the University of Washington and the National Science Foundation (MRI-1624430).

* These two authors contributed equally.
† xsli@uw.edu

[1] D. Mocatta, G. Cohen, J. Schattner, O. Millo, E. Rabani, and U. Banin, Science **332**, 77 (2011).
[2] M. Sytnyk, R. Kirchschlager, M. I. Bodnarchuk, D. Primetzhofer, D. Kriegner, H. Enser, J. Stangl, P. Bauer, M. Voith, A. W. Hassel, F. Krumeich, F. Ludwig, A. Meingast, G. Kothleitner, M. V. Kovalenko, and W. Heiss, Nano Lett. **13**, 586 (2013).
[3] S. Pezzagna, D. Rogalla, D. Wildanger, J. Meijer, and A. Zaitsev, New J. Phys. **13**, 035024 (2011).
[4] J. Eilers, E. Groeneveld, C. de Mello Donegá, and A. Meijerink, J. Phys. Chem. Lett. **3**, 1663 (2012).
[5] F. Dolde, M. W. Doherty, J. Michl, I. Jakobi, B. Naydenov, S. Pezzagna, J. Meijer, P. Neumann, F. Jelezko, N. B. Manson, and J. Wrachtrup, Phys. Rev. Lett. **112**, 097603 (2014).
[6] J. L. Stein, M. I. Steimle, M. W. Terban, A. Petrone, S. J. L. Billinge, X. Li, and B. M. Cossairt, Chem. Mater. **29**, 7984 (2017).
[7] M. E. Levinshteĭn, S. L. Rumyantsev, and M. Shur, *Handbook Series on Semiconductor Parameters: Si, Ge, C (Diamond), GaAs, GaP, GaSb, InAs, InP, InSb* (World Scientific Publishing, Singapore, 1996).
[8] K. Holt, Phil. Trans. R. Soc. A **365**, 2845 (2007).
[9] G. Balasubramanian, I. Chan, R. Kolesov, M. Al-Hmoud, J. Tisler, C. Shin, C. Kim, A. Wojcik, P. Hemmer, A. Krueger, T.Hanke, A. Leitenstorfer, R. Bratschitsch, F. Jelezko, and J. Wrachtrup, Nature **455**, 648 (2008).
[10] Y.-R. Chang, H.-Y. Lee, K. Chen, C.-C. Chang, D.-S. Tsai, C.-C. Fu, T.-S. Lim, Y.-K. Tzeng, C.-Y. Fang, C.-C. Han, H.-C. Chang, and W. Fann, Nat. Nanotechnol. **3**, 284 (2008).
[11] L. Mc Guinness, Y. Yan, A. Stacey, D. Simpson, L. Hall, D. Maclaurin, S. Prawer, P. Mulvaney, J. Wrachtrup, F. Caruso, R. E. Scholten, and L. C. L. Hollenberg, Nat. Nanotechnol. **6**, 358 (2011).
[12] P. J. Pauzauskie, J. C. Crowhurst, M. A. Worsley, T. A. Laurence, A. L. D. Kilcoyne, Y. Wang, T. M. Willey, K. S. Visbeck, S. C. Fakra, W. J. Evans, J. M. Zaug, and J. H. Satcher, Proc. Natl. Acad. Sci. U.S.A. **108**, 8550 (2011).
[13] S. Manandhar, P. B. Roder, J. L. Hanson, M. Lim, B. E. Smith, A. Mann, and P. J. Pauzauskie, J. Mater. Res. **29**, 2905 (2014).
[14] N. Aslam, M. Pfender, P. Neumann, R. Reuter, A. Zappe, F. F. de Oliveira, A. Denisenko, H. Sumiya, S. Onoda, J. Isoya, and J. Wrachtrup, Science , eaam8697 (2017).
[15] C. Kittel and P. McEuen, *Introduction to Solid State Physics*, Vol. 8 (Wiley, New York, NY, 1976).
[16] N. Ashcroft and N. Mermin, *Solid State Physics* (Saunders College, Philadelphia, PA, 1976).
[17] L. E. Brus, J. Chem. Phys. **80**, 4403 (1984).
[18] M. G. Bawendi, M. L. Steigerwald, and L. E. Brus, Annu. Rev. Phys. Chem. **41**, 477 (1990).
[19] T. Karin, S. Dunham, and K.-M. Fu, Appl. Phys. Lett. **105**, 053106 (2014).
[20] M. Drake, E. Scott, and J. Reimer, New J. Phys. **18**, 013011 (2015).
[21] K. Sasaki, E. E. Kleinsasser, Z. Zhu, W.-D. Li, H. Watanabe, K.-M. C. Fu, K. M. Itoh, and E. Abe, Appl. Phys. Lett. **110**, 192407 (2017).
[22] A. Petrone, J. J. Goings, and X. Li, Phys. Rev. B **94**, 165402 (2016).
[23] M. Leifgen, T. Schröder, F. Gödeke, R. Riemann, V. Metillon, E. Neu, C. Hepp, C. Arend, C. Becher, K. Lauritsen, and O. Benson, New J. Phys. **16**, 023021 (2014).
[24] E. Neu, D. Steinmetz, J. Riedrich-Möller, S. Gsell, M. Fischer, M. Schreck, and C. Becher, New J. Phys. **13**, 025012 (2011).
[25] A. Dietrich, K. D. Jahnke, J. M. Binder, T. Teraji, J. Isoya, L. J. Rogers, and F. Jelezko, New J. Phys. **16**, 113019 (2014).
[26] M. Crane, A. Petrone, R. A. Beck, M. Lim, X. Zhou, X. Li, R. M. Stroud, and P. Pauzauskie, arxiv , https://arxiv.org/abs/1804.00350 (2018).
[27] J. Goss, R. Jones, S. J. Breuer, P. R. Briddon, and S. Öberg, Phys. Rev. Lett. **77**, 3041 (1996).
[28] J. Goss, P. Briddon, and M. Shaw, Phys. Rev. B **76**, 075204 (2007).
[29] A. S. Zyubin, A. Mebel, M. Hayashi, H. C. Chang, and S. H. Lin, J. Comput. Chem. **30**, 119 (2009).
[30] A. Gali and J. R. Maze, Phys. Rev. B **88**, 235205 (2013).
[31] L. J. Rogers, K. D. Jahnke, M. W. Doherty, A. Dietrich, L. P. Mc Guinness, C. Müller, T. Teraji, H. Sumiya, J. Isoya, N. B. Manson, and F. Jelezko, Phys. Rev. B **89**, 235101 (2014).
[32] T. Müller, C. Hepp, B. Pingault, E. Neu, S. Gsell, M. Schreck, H. Sternschulte, D. Steinmüller-Nethl, C. Becher, and M. Atatüre, Nat. Commun. **5**, 3328 (2014).
[33] I. I. Vlasov, A. A. Shiryaev, T. Rendler, S. Steinert, S.-Y. Lee, D. Antonov, M. Vörös, F. Jelezko, A. V. Fisenko, L. F. Semjonova, , J. Biskupek, U. Kaiser, O. I. Lebedev, I. Sildos, P. R. Hemmer, V. I. Konov, A. Gali, and J. Wrachtrup, Nat. Nanotechnol. **9**, 54 (2014).
[34] C. D. Clark, H. Kanda, I. Kiflawi, and G. Sittas, Phys. Rev. B **51**, 16681 (1995).
[35] E. Neu, C. Hepp, M. Hauschild, S. Gsell, M. Fischer, H. Sternschulte, D. Steinmüller-Nethl, M. Schreck, and C. Becher, New J. Phys. **15**, 043005 (2013).
[36] C. Hepp, T. Müller, V. Waselowski, J. N. Becker, B. Pingault, H. Sternschulte, D. Steinmüller-Nethl, A. Gali, J. R. Maze, M. Atatüre, and C. Becher, Phys. Rev. Lett. **112**, 036405 (2014).
[37] G. Thiering and A. Gali, arxiv , https://arxiv.org/abs/1804.07004 (2018).
[38] S. L. Chang, A. S. Barnard, C. Dwyer, C. B. Boothroyd, R. K. Hocking, E. Ōsawa, and R. J. Nicholls, Nanoscale **8**, 10548 (2016).
[39] E. Badaeva, C. M. Isborn, Y. Feng, S. T. Ochsenbein, D. R. Gamelin, and X. Li, J. Phys. Chem. C **113**, 8710 (2009).
[40] R. Beaulac, Y. Feng, J. W. May, E. Badaeva, D. R. Gamelin, and X. Li, Phys. Rev. B **84**, 195324 (2011).
[41] J. W. May, R. J. McMorris, and X. Li, J. Phys. Chem. Lett. **3**, 1374 (2012).
[42] J. W. May, J. Ma, E. Badaeva, and X. Li, J. Phys. Chem. C **118**, 13152 (2014).
[43] J. J. Goings, A. M. Schimpf, J. W. May, R. W. Johns, D. R. Gamelin, and X. Li, J. Phys. Chem. C **118**, 26584 (2014).

[44] B. Peng, J. W. May, D. R. Gamelin, and X. Li, J. Phys. Chem. C **118**, 7630 (2014).
[45] L. R. Bradshaw, J. W. May, J. L. Dempsey, X. Li, and D. R. Gamelin, Phys. Rev. B **89**, 115312 (2014).
[46] E. Q. Chong, D. B. Lingerfelt, A. Petrone, and X. Li, J. Phys. Chem. C **120**, 19434 (2016).
[47] D. C. Gary, A. Petrone, X. Li, and B. M. Cossairt, Chem. Commun. **53**, 161 (2017).
[48] R. Beck, A. Petrone, J. M. Kasper, M. J. Crane, P. J. Pauzauskie, and X. Li, J. Phys. Chem. C **122**, 8573 (2018).
[49] M. W. Wong, Chem. Phys. Lett. **256**, 391 (1996).
[50] V. Barone, J. Bloino, and M. Biczysko, Phys. Chem. Chem. Phys. **12**, 1092 (2010).
[51] A. Petrone, D. B. Lingerfelt, D. B. Williams-Young, and X. Li, J. Phys. Chem. Lett. **7**, 4501 (2016).
[52] G. Donati, D. B. Lingerfelt, A. Petrone, N. Rega, and X. Li, J. Phys. Chem. A **120**, 7255 (2016).
[53] D. B. Lingerfelt, D. B. Williams-Young, A. Petrone, and X. Li, J. Chem. Theory Comput. **12**, 935 (2016).
[54] N. R. Greiner, D. S. Phillips, J. D. Johnson, and F. Volk, Nature , 440 (1988).
[55] V. Y. Dolmatov, Russ. Chem. Rev. **76**, 339 (2007).
[56] E. Ōsawa, Pure Appl. Chem. **80**, 1365 (2008).
[57] K. Takahashi, A. Yoshikawa, and A. Sandhu, *Wide Bandgap Semiconductors: Fundamental Properties and Modern Photonic and Electronic Devices* (Springer, New York, NY, 2007).
[58] S. S. Moliver, Tech. Phys. **48**, 1449 (2003).
[59] T. Feng and B. D. Schwartz, J. Appl. Phys. **73**, 1415 (1993).
[60] G. Thiering and A. Gali, Phys. Rev. B **92**, 165203 (2015).
[61] M. J. Frisch, G. W. Trucks, H. B. Schlegel, G. E. Scuseria, M. A. Robb, J. R. Cheeseman, G. Scalmani, V. Barone, G. A. Petersson, H. Nakatsuji, X. Li, M. Caricato, A. V. Marenich, J. Bloino, B. G. Janesko, R. Gomperts, B. Mennucci, H. P. Hratchian, J. V. Ortiz, A. F. Izmaylov, J. L. Sonnenberg, D. Williams-Young, F. Ding, F. Lipparini, F. Egidi, J. Goings, B. Peng, A. Petrone, T. Henderson, D. Ranasinghe, V. G. Zakrzewski, J. Gao, N. Rega, G. Zheng, W. Liang, M. Hada, M. Ehara, K. Toyota, R. Fukuda, J. Hasegawa, M. Ishida, T. Nakajima, Y. Honda, O. Kitao, H. Nakai, T. Vreven, K. Throssell, J. A. Montgomery, Jr., J. E. Peralta, F. Ogliaro, M. J. Bearpark, J. J. Heyd, E. N. Brothers, K. N. Kudin, V. N. Staroverov, T. A. Keith, R. Kobayashi, J. Normand, K. Raghavachari, A. P. Rendell, J. C. Burant, S. S. Iyengar, J. Tomasi, M. Cossi, J. M. Millam, M. Klene, C. Adamo, R. Cammi, J. W. Ochterski, R. L. Martin, K. Morokuma, O. Farkas, J. B. Foresman, and D. J. Fox, "Gaussian Development Version Revision I.10++," Gaussian Inc., Wallingford CT 2016.
[62] A. D. Becke, J. Chem. Phys. **98**, 5648 (1993).
[63] C. Lee, W. Yang, and R. G. Parr, Phys. Rev. B **37**, 785 (1988).
[64] B. Miehlich, A. Savin, H. Stoll, and H. Preuss, Chem. Phys. Lett. **157**, 200 (1989).
[65] T. Yanai, D. P. Tew, and N. C. Handy, Chem. Phys. Lett. **393**, 51 (2004).
[66] M. Vörös and A. Gali, Phys. Rev. B **80**, 161411(R) (2009).
[67] T. Demján, M. Vörös, M. Palummo, and A. Gali, J. Chem. Phys. **141**, 064308 (2014).
[68] M. Kaviani, P. Deák, B. Aradi, T. Frauenheim, J.-P. Chou, and A. Gali, Nano Lett. **14**, 4772 (2014).
[69] C.-K. Lin, Y.-H. Wang, H.-C. Chang, M. Hayashi, and S. H. Lin, J. Chem. Phys. **129**, 124714 (2008).
[70] A. Gali, Phys. Status Solidi B **248**, 1337 (2011).
[71] N. Mardirossian, J. A. Parkhill, and M. Head-Gordon, Phys. Chem. Chem. Phys. **13**, 19325 (2011).
[72] A. D. Laurent and D. Jacquemin, Int. J. Quant. Chem. **113**, 2019 (2017).
[73] R. Derian, K. Tokár, B. Somogyi, A. Gali, and I. Štich, J. Chem. Theory Comput. **13**, 6061 (2017).
[74] M. E. Casida, *Recent Advances in Density Functional Methods:(Part I)*, edited by D. P. Chong, Vol. 1 (World Scientific Publishing, Singapore, 1995) pp. 155–193.
[75] A. Dreuw and M. Head-Gordon, Chem. Rev. **105**, 4009 (2005).
[76] R. E. Stratmann, G. E. Scuseria, and M. J. Frisch, J. Chem. Phys. **109**, 8218 (1998).
[77] W. Liang, S. A. Fischer, M. J. Frisch, and X. Li, J. Chem. Theory Comput. **7**, 3540 (2011).
[78] P. J. Lestrange, P. D. Nguyen, and X. Li, J. Chem. Theory Comput. **11**, 2994 (2015).
[79] See Supplemental Material at [*URL will be inserted by publisher*] for the change of the SiV structure for full-diamond optimization, the isotropic effects of the silicon on the Raman spectroscopy, and enlarged images of the normal modes displayed in FIG. 8.
[80] H.-P. Komsa, T. T. Rantala, and A. Pasquarello, Phys. Rev. B **86**, 045112 (2012).
[81] S. Vepřek, Thin Solid Films **297**, 145 (1997).
[82] E. Badaeva, Y. Feng, D. R. Gamelin, and X. Li, New J. Phys. **10**, 055013 (2008).
[83] H. Sternschulte, K. Thonke, J. Gerster, W. Limmer, R. Sauer, J. Spitzer, and P. Münzinger, Diamond Relat. Mater. **4**, 1189 (1995).
[84] E. Neu, M. Fischer, S. Gsell, M. Schreck, and C. Becher, Phys. Rev. B **84**, 205211 (2011).
[85] S. W. Brown and S. C. Rand, J. Appl. Phys. **78**, 4069 (1995).
[86] S. Salustro, A. Erba, C. M. Zicovich-Wilson, Y. Nöel, L. Maschio, and R. Dovesi, Phys. Chem. Chem. Phys. **18**, 21288 (2016).
[87] J. Bielecki and E. W. Lipiec, J. Bioinfo. Comp. Bio. **14**, 1650002 (2016).
[88] J. R. Cheeseman and M. J. Frisch, J. Chem. Theory Comput. **7**, 3323 (2011).
[89] F. Billes, J. Mol. Struct. **339**, 15 (1995).
[90] J. Filik, J. N. Harvey, N. Allan, P. May, J. Dahl, S. Liu, and R. Carlson, Phys. Rev. B **74**, 035423 (2006).
[91] S. Prawer and R. J. Nemanich, Proc. R. Soc. London, Ser. A **362**, 2537 (2004).
[92] J. Cebik, J. K. McDonough, F. Peerally, R. Medrano, I. Neitzel, Y. Gogotsi, and S. Osswald, Nanotechnology **24**, 205703 (2013).
[93] V. I. Korepanov, H. o Hamaguchi, E. Osawa, V. Ermolenkov, I. K. Lednev, B. J. Etzold, O. Levinson, B. Zousman, C. P. Epperla, and H.-C. Chang, Carbon **121**, 322 (2017).
[94] W. Li, S. Irle, and H. A. Witek, ACS Nano **4**, 4475 (2010).
[95] G. Wan, P. Yang, R. K. Fu, Y. Mei, T. Qiu, S. Kwok, J. P. Ho, N. Huang, X. Wu, and P. K. Chu, Diamond Relat. Mater. **15**, 1276 (2006).
[96] S.-l. Chen, S. Bin, J.-G. Zhang, W. Liang, and F.-H. Sun, Trans. Nonferrous Met. Soc. China **22**, 3021 (2012).
[97] Y.-X. Cui, J.-G. Zhang, F.-H. Sun, and Z.-M. Zhang, Trans. Nonferrous Met. Soc. China **23**, 2962 (2013).

[98] M. Berglund and M. E. Wieser, Pure Appl. Chem. **83**, 397 (2011).
[99] H. Moseley, Lond. Edinb. Dubl. Phil. Mag. **26**, 1024 (1913).
[100] H. Moseley, Lond. Edinb. Dubl. Phil. Mag. **27**, 703 (1914).
[101] J. Stöhr, *NEXAFS Spectroscopy* (Springer-Verlag: Berlin, Heidelberg, 1992).
[102] A. Nilsson and L. G. M. Pettersson, Surf. Sci. Rep. **55**, 49 (2004).